A Numerical Tool for Quantitative Analysis of Ionic-Liquid Ion Source Time-of-Flight Data

IEPC-2024-406

Presented at the 38th International Electric Propulsion Conference, Toulouse, France
June 23-28, 2024

Oliver Jia-Richards*
University of Michigan, Ann Arbor, Michigan, 48105, U.S.A.

This paper builds on prior work by presenting an updated numerical tool that allows for quantitative estimation of the species composition in the plume of an ionic-liquid ion source operating in the ion mode from time-of-flight data. Given an experimentally-measured time-of-flight curve, our tool estimates the current fraction of ions and ion clusters in the ionic-liquid ion source plume, enabling quantitative comparison of time-of-flight data collected at different operating conditions. A key update to the tool is the estimation of a finite-width energy distribution for primary species—particles that do not fragment in the source acceleration region—whereas the prior work assumed that the energy distribution of primary species was monoenergetic. The estimated finite-width energy distribution is able to better explain the sloped nature of time-of-flight curves at the arrival times of primary species relative to large detector response times, and agrees well with experimental measurements of the particle energy distribution. Finally, we demonstrate an application of the numerical tool for analyzing the angular and transient dependence of the species composition for an ionic-liquid ion source with a single porous carbon emitter.

I. Introduction

Time-of-flight mass spectrometry is one of the primary experimental methods for indirectly characterizing the performance of ionic-liquid ion sources. The principle behind time-of-flight mass spectrometry is that the speeds of charged particles emitted by an ionic-liquid ion source are dependent on the acceleration potential, common to all particles, and the particles' charge-to-mass ratios, unique to each particle species. By measuring the flight times of charged particles across a known distance, the speeds of the particles can be estimated which in turn provides an estimate of the particles' charge-to-mass ratios. The estimated charge-to-mass ratios are often directly translated to particle masses as the particles emitted by an ionic-liquid ion source are typically assumed to be singly charged.

Knowledge about the mass distribution of particles emitted by an ionic-liquid ion source through time-of-flight mass spectrometry enables indirect estimation of the thrust output and specific impulse. The most common approach is to integrate raw or time-filtered time-of-flight data over the measured particle flight times since the change in measured current at each flight time corresponds to the fraction of the emitted beam composed of particles with the corresponding charge-to-mass ratio [1]. The integration approaches provide species-averaged metrics for the thrust output, specific impulse, and overall mass distribution. However, in some scenarios the fraction of individual particle species in the beam are desired. Ionic-liquid ion sources operating in the ion mode predominantly emit a discrete set of ions and ion clusters. Ion clusters are known to fragment post-emission [2], which will produce low-energy ions that can impact system integration considerations such as spacecraft charging [3].

Prior methods for extracting the relative composition of different ions or ion clusters in the emitted beam have primarily been qualitative, and approaches for quantifying the relative species composition have been based on visual inspection of the time-of-flight data [4], which can be imprecise. Future interest in making comparisons in the species composition for different operating conditions, such as characterizing the transient

*Assistant Professor, Department of Aerospace Engineering, oliverjr@umich.edu.

response of ionic-liquid ion sources, necessitates the development of rigorous numerical methods for properly quantifying the beam species composition. This work builds on prior work that demonstrated the ability to numerically estimate the current fraction of different species in an ionic-liquid ion source plume, from monomers up to heptamers, using an ensemble Kalman update approach [5]. Here, we specifically focus on the impact of the energy distribution of primary species—particles that do not fragment in the source acceleration region—on the time-of-flight data.

This paper details a nonlinear least squares approach to estimating the current fractions of ions and ion clusters in an ionic-liquid ion source plume as well as the energy distribution of primary species from time-of-flight data. The method relies on the ability to simulate time-of-flight data given assumed species current fractions as well as primary species energy distribution with a forward model. We demonstrate that incorporating a finite-width energy distribution for primary species in the plume is able to well represent the sloped nature of time-of-flight curves at the arrival times of primary species. This is in contrast to our prior approach which assumed that the lag in the time-of-flight data was caused by the finite response time of the detector [5]. Estimates of the energy distribution that best explains experimental time-of-flight data is in good agreement with experimental measurements of the energy distribution, albeit with a greater fraction of low-energy ions. The final portion of this paper leverages the numerical tool to analyze the angular and transient dependence of the species composition for an ionic-liquid ion source with a single porous carbon emitter. Through the use of our tool, we are able to quantitatively compare the current fraction of different species of the beam for different off-axis angles or delay times after emission startup.

II. Methodology

The estimation approach used in this work is nonlinear least squares estimation. In the general case, we assume that we have a measurement vector, $\boldsymbol{y}$, that is related to a parameter vector, $\boldsymbol{x}$, through a forward model, $\boldsymbol{h}(\boldsymbol{x})$, according to

$$\boldsymbol{y} = \boldsymbol{h}(\boldsymbol{x}) + \boldsymbol{\nu} \tag{1}$$

where $\boldsymbol{\nu}$ is normally-distributed additive measurement noise with covariance matrix $[\Sigma_{\boldsymbol{\nu}}]$. Given the forward model and a parameter vector of interest, it is easy to simulate the corresponding measurement vector. For the time-of-flight case, the parameter vector would contain assumed values of the current fractions for different species in the beam as well as other parameters of interest while the measurement vector would correspond to the detector current magnitude at different flight times. The forward model therefore represents some function that can simulate a time-of-flight curve given assumed values for the parameters.

In nonlinear least squares estimation we are not interested in determining $\boldsymbol{y}$ from $\boldsymbol{x}$, but rather estimating the parameter vector $\boldsymbol{x}^*$ that best explains an observed measurement vector $\boldsymbol{y}^*$. The estimation process is iterative, where the guess for the parameter vector, $\boldsymbol{x}_i$, is updated to a new guess, $\boldsymbol{x}_{i+1}$, according to

$$\boldsymbol{x}_{i+1} = \boldsymbol{x}_i + \Delta\boldsymbol{x}_i \tag{2}$$

The parameter vector update, $\Delta\boldsymbol{x}_i$, is calculated according to

$$\Delta\boldsymbol{x}_i = \left([H(\boldsymbol{x}_i)]^T[\Sigma_{\boldsymbol{\nu}}][H(\boldsymbol{x}_i)]\right)^{-1}[H(\boldsymbol{x}_i)]^T[\Sigma_{\boldsymbol{\nu}}]^{-1}(\boldsymbol{y}^* - \boldsymbol{h}(\boldsymbol{x}_i)) \tag{3}$$

where $[H(\boldsymbol{x}_i)]$ is the linearized measurement matrix calculated as the Jacobian of $\boldsymbol{h}$ evaluated at the current guess for the parameter vector

$$[H(\boldsymbol{x}_i)] = \nabla_{\boldsymbol{x}}\boldsymbol{h}(\boldsymbol{x})\big|_{\boldsymbol{x}_i} \tag{4}$$

Since in practice an analytical solution to Eq. 4 is not available, we approximate $[H(\boldsymbol{x}_i)]$ numerically. The j^{th} column of $[H(\boldsymbol{x}_i)]$ can be approximated through a finite-difference approach

$$[H(\boldsymbol{x}_i)]_{:,j} \approx \frac{1}{\epsilon}\left(\boldsymbol{h}(\boldsymbol{x}_i + \boldsymbol{\epsilon}_j) - \boldsymbol{h}(\boldsymbol{x}_i)\right) \tag{5}$$

where $\boldsymbol{\epsilon}_j$ is a vector of length $n+1$ where all elements are zero except for the j^{th} element which is equal to a small perturbation, ϵ. Finally, the covariance matrix representing the uncertainty in the parameter vector at each guess can be calculated from

$$[\Sigma_{\boldsymbol{x}}(\boldsymbol{x}_i)] = \left([H(\boldsymbol{x}_i)]^T[\Sigma_{\boldsymbol{\nu}}][H(\boldsymbol{x}_i)]\right)^{-1} \tag{6}$$

The 38th International Electric Propulsion Conference, P. Baudis Convention Center, Toulouse, France, June 23-28, 2024

Algorithm 1 Nonlinear Least Squares Estimation

Given observed measurement vector, $\boldsymbol{y}^*$
Initialize parameter vector guess, $\boldsymbol{x}$
while number of iterations is less than the maximum number of iterations **do**
    Approximate the linearized measurement matrix, $[H]$, using Eq. 5
    Calculate the parameter vector update, $\Delta\boldsymbol{x}$, from Eq. 3
    Update the parameter vector guess, $\boldsymbol{x}$, using Eq. 2
    Calculate the parameter vector covariance, $[\Sigma_{\boldsymbol{x}}]$, from Eq. 6
    if convergence criterion in Eq. 7 is satisfied **then**
        Exit update loop
return parameter vector estimate, $\boldsymbol{x}$, and corresponding covariance, $[\Sigma_{\boldsymbol{x}}]$

The guess for the parameter vector is continuously updated with Eq. 2 until either a maximum number of iterations or a specified convergence criterion is met. In this work, the convergence criterion checks if the squared change in each element of the parameter vector is less than its corresponding marginal variance

$$\Delta\boldsymbol{x}_j^2 < [\Sigma_{\boldsymbol{x}}(\boldsymbol{x}_i)]_{jj} \qquad \forall j \in \{1, \ldots, n\} \tag{7}$$

where it is assumed that the parameter vector contains n elements. If this convergence criterion is met, then our uncertainty in each of the parameters is greater than the change in the parameter estimate between iterations. Therefore, there is little advantage in continuing to update the parameter vector guess. The nonlinear least squares estimation algorithm is summarized in Algorithm 1 for arbitrary parameter and measurement vectors as well as corresponding forward model.

III. Forward Model

Crucial to our ability to use nonlinear least squares estimation for processing time-of-flight data is a defined forward model, $\boldsymbol{h}(\boldsymbol{x})$. In this work we assume that the parameter vector is composed of the current fractions of different species of interest as well as the minimum, maximum, and midpoint values of a triangular distribution that defines the energy distribution for unfragmented, primary species. The parameter vector is therefore

$$\boldsymbol{x} = \begin{bmatrix} \alpha_1 & \ldots & \alpha_s & \Delta V_{\text{min}} & \Delta V_{\text{max}} & \Delta V_{\text{mid}} \end{bmatrix}^T \tag{8}$$

where α_k is the current fraction of species $k \in \{1, \ldots, s\}$ with a total of s species of interest and ΔV_{min}, ΔV_{max}, and ΔV_{mid} correspond to the difference between the minimum, maximum, and midpoint of the triangular energy distribution relative to the source potential. If $\Delta V_{\text{min}} = \Delta V_{\text{max}} = \Delta V_{\text{mid}} = 0$ then the beam is monoenergetic with energy equal to the source potential while negative values of ΔV_{min}, ΔV_{max}, and ΔV_{mid} correspond to energy deficits in the beam.

The species in the parameter vector can represent either primary species, those that do not fragment prior to emission, or secondary species, those that result from fragmentation prior to emission. It is assumed here that fragmentation always reduces the degree of solvation of the particle by one (i.e., trimers can only fragment into dimers), and that fragmentation products do not fragment again prior to emission. All primary species are assigned a charge-to-mass ratio determined by the ionic liquid and the degree of solvation of the species. All secondary species are assigned two charge-to-mass ratios: one for the initial charge-to-mass ratio prior to fragmentation and another for the final charge-to-mass ratio after fragmentation. If species k represents a secondary species, then it is assumed that all particles of species k fragment prior to leaving the thruster. The fragmentation is assumed to be constant with respect to potential; if the thruster potential is V then the fraction of species k that fragments at potentials less than some $V' < V$ is given by V'/V.

The baseline forward model to take a parameter vector and simulate the corresponding time-of-flight data is outlined in Ref. [5]. The difference in this work is that primary species are now assigned a triangular energy distribution defined by ΔV_{min}, ΔV_{max}, and ΔV_{mid}, which means that primary species do not all arrive at the time-of-flight detector at the same time. The exhaust speed of a primary-species particle is given by

$$c = \sqrt{2q_k(V + \Delta V)/m_k}$$

The 38th International Electric Propulsion Conference, P. Baudis Convention Center, Toulouse, France, June 23-28, 2024

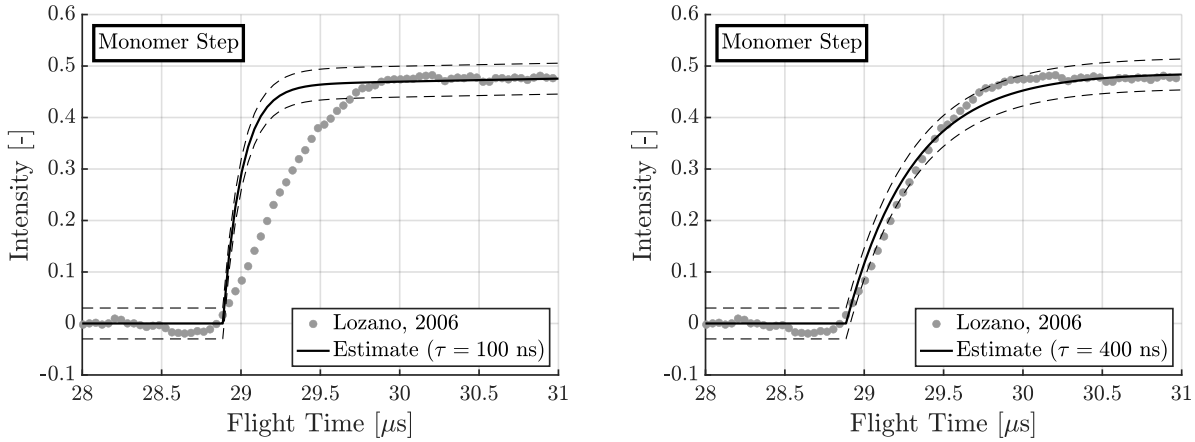

Figure 1 Comparison of experimental, from Ref. [6], and estimated time-of-flight curves at the monomer step for assumed time-of-flight detector response times of 100 ns (left) and 400 ns (right).

where q_k and m_k are the species charge and mass, and ΔV is distributed according to a triangular distribution with minimum, maximum, and midpoint given by ΔV_{min}, ΔV_{max}, and ΔV_{mid}. The distribution of exhaust speeds can be converted into a distribution of arrival times of primary species at the time-of-flight detector. The change in the forward model is that the contribution of primary species to the simulated time-of-flight data is no longer a step function (prior to accounting for the detector response time) as assumed in Ref. [5], but rather distributed around the expected arrival time of each primary species.

Figure 1 shows the reason for including the energy distribution to the forward model. Both plots show a comparison of experimental time-of-flight data, from Ref. [6], and simulated time-of-flight data using a forward model that assumes all primary species are monoenergetic near the monomer step. The difference between the two plots is in the assumed rise time of the time-of-flight detector. A rise time of 100 ns is closer to the expected rise time of the detector, but cannot explain the sloped nature of the monomer step. A rise time of 400 ns more closely matches the time scale of the monomer step, but does show some qualitative differences relative to the experimental data. If the energy distribution of primary species is not accounted for, then the time scale of the monomer step can only be explained through a higher-than-expected detector response time, and shows qualitative differences relative to the experimental data.

Figure 2 shows a comparison of experimental time-of-flight data, from Ref. [6], and simulated time-of-flight data using a forward model that accounts for an energy distribution near the monomer step. The parameters of the energy distribution (ΔV_{min}, ΔV_{max}, and ΔV_{mid}) are estimated in order to best explain the experimental data. We can see that relative to Figure 1, the simulated time-of-flight data better explains the sloped shape of the monomer step. Also shown in Figure 2 is the estimated energy distribution compared to the measured energy distribution also presented in Ref. [6]. The estimated energy distribution is shifted by +7 eV for the comparison as the time-of-flight data was taken with an acceleration potential of 993 V while the particle energy data was taken with an acceleration potential of 1000 V. We can see that the estimated energy distribution matches the experimental data quite well, particularly at higher energies. The estimated energy distribution does include a greater proportion of lower-energy particles than the experimental data in order to explain the time-of-flight data. This discrepancy is currently being investigated.

Figure 3 shows a similar comparison to Figure 2 but near the dimer step rather than the monomer step. The estimated energy distribution that best explains the dimer step still closely matches the experimental energy distribution, but does have a noticeable positive shift compared to the monomer energy distribution in Figure 2. This discrepancy is also being investigated. A notable challenge for this comparison is that the experimental energy distributions are for all particles in the beam, while the estimated energy distributions can be evaluated for specific species. The parameters for the estimated energy distributions that best explain the monomer and dimer steps are shown in Table 1. Considering only the monomer step, the estimated energy distribution shows a midpoint energy deficit in the beam of -5.9 V, consistent with energy deficit reported in Ref. [6]. The range of the estimated energy distribution extends down to -72.4 V and up to +8.4 V which is in line with the overall range of the experimental energy distribution.

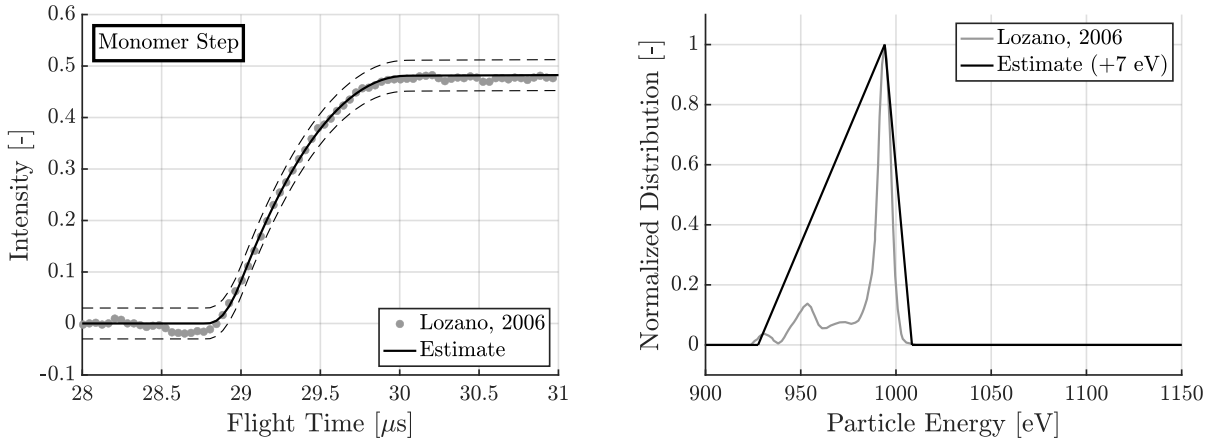

Figure 2 Comparison of experimental, from Ref. [6], and estimated time-of-flight curves at the monomer step (left) and corresponding estimated particle energy distribution (right).

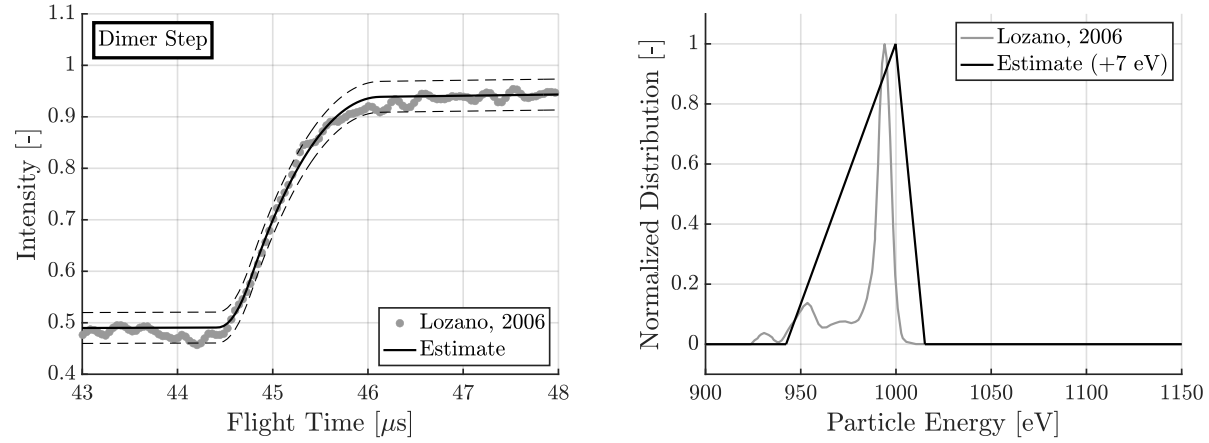

Figure 3 Comparison of experimental, from Ref. [6], and estimated time-of-flight curves at the dimer step (left) and corresponding estimated particle energy distribution (right).

IV. Composition Comparison

The purpose of the numerical tool is to quantify the current fraction of different species of interest in the emitted beam. The ability to quantify the species composition from time-of-flight data enables direct comparison of the species composition for different operating points or other parameters that might change the beam composition. Two parameters of interest might be the dependence of the species composition on off-axis angle and the startup transient of an ionic-liquid ion source. Experimental time-of-flight data, described in Ref. [7], was taken for a porous carbon emitter at various off-axis angles. Additional experimental data was taken during the startup transient, to analyze the transient behavior of the beam composition. No discussion regarding the cause of the dependence of the species composition on off-axis angle or startup transient is provided here as the main purpose of this paper is simply to present the numerical tool.

The species of interest were monomers, dimers, trimers, and "heavy" clusters representing all ion clusters heavier than a trimer (i.e., tetramers and above). Both primary and secondary versions of each species were considered, where the secondary version of the species indicates that it was the product of a fragmentation event from the next-heaviest species (i.e., secondary monomers result from the fragmentation of dimers). For the purposes of data presentation, the current fractions for each species are presented based on the species that was emitted. For example, the presented current fraction of "trimers" is the sum of both primary trimers and secondary dimers since a secondary dimer was initially emitted as a trimer before fragmentation.

Table 1 Estimated triangular energy distribution parameters.

	ΔV_{min} [V]	ΔV_{max} [V]	ΔV_{mid} [V]
Monomer step	-72.4 ± 2.5	8.4 ± 4.5	-5.9 ± 4.9
Dimer step	-57.5 ± 2.2	15.2 ± 3.4	0.2 ± 3.7

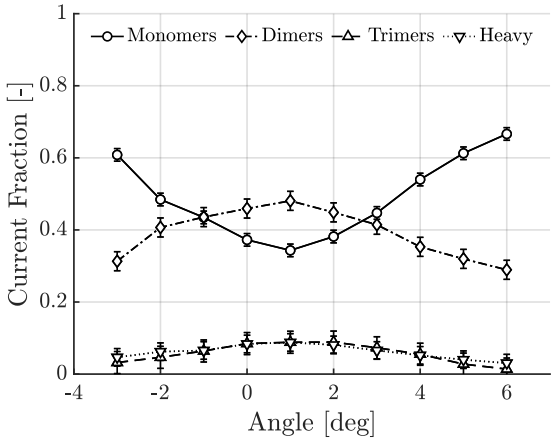

Figure 4 Estimated particle species current fraction versus off-axis angle for an ionic-liquid ion source with a single porous carbon emitter. Heavy refers all particles heavier than a trimer.

Figure 4 shows the current fraction of different species versus angle for a porous carbon emitter using EMI-BF_4 with emitter-extractor potential of 800 V and emission current of 10 nA operated in the positive polarity. Time-of-flight data were taken at increments of 1° about a single rotational axis and then processed using the numerical tool described in this work. Error bars show 3σ uncertainty in the current fraction. The central axis of the beam is offset by approximately +1° from the "on-axis" angle. Whether or not this is due to off-axis firing of the emitter or simply a misalignment in the experimental setup is unclear. The species composition along the central axis of the beam is approximately 34% monomers, 48% dimers, 9% trimers, and 9% heavy species. As we move away from the central axis, the relative fraction of monomers increases while the relative fractions of dimers, trimers, and heavy species decreases. At the outer edges of the beam (+6°) the species composition is 67% monomers, 29% dimers, 1% trimers, and 3% heavy species.

One implication of this data worth noting here is in the use of time-of-flight data for indirect estimation of the thrust and specific impulse of an electrospray thruster. In many experimental studies time-of-flight data is only sampled at a single angle, typically the expected central axis of the thruster. The species composition clearly depends on angle. Therefore, only sampling along the central axis may give a skewed estimate of thrust and specific impulse. For this particular emitter and operating point, sampling along the central axis would result in a higher estimated thrust and lower specific impulse relative to sampling away from the central axis. Care must be taken when obtaining indirect estimates of the thrust and specific impulse of an electrospray thruster when relying on time-of-flight data to account for these angular dependencies.

Figure 5 shows the current fraction of different species during the startup transient of the porous carbon emitter using the method described in Ref. [8]. The gate delay indicates the time after the onset of emission at which the time-of-flight gate is opened for a short period of time in order to sample the beam at a given time after emission start. All data is taken at the expected central axis of the beam, though Figure 4 demonstrates that this may not correspond to the actual central axis of the beam. Data were taken for two cases: one where the polarity of the emitter was alternated at 1 Hz and another where the polarity of the emitter was alternated at 10 Hz. Only the data taken in the positive polarity is presented here. The lines show exponential fits to the current fraction of each species as a function of gate delay.

The interesting result of Figure 5 is that the species composition of the beam clearly changes during the startup transient of the emitter, and that the behavior of the species composition is different for the two polarity alternation frequencies. When alternating at 1 Hz the average mass flow rate of the beam increases

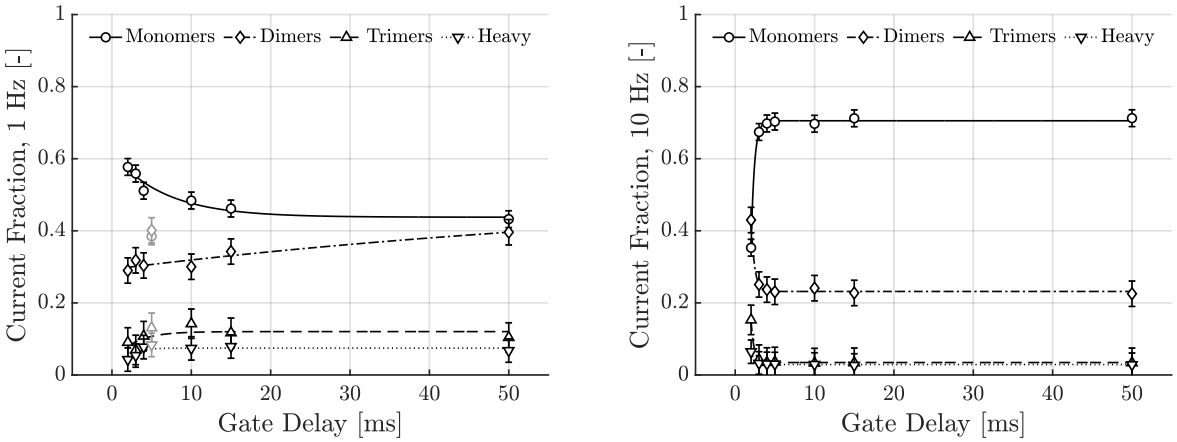

Figure 5 Estimated particle species current fraction versus time post emission startup for an ionic-liquid ion source with a single porous carbon emitter and polarity alternation of 1 Hz (left) and 10 Hz (right). Heavy refers to all particles heavier than a trimer.

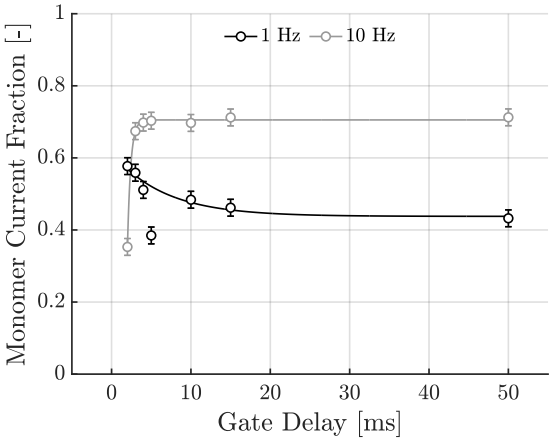

Figure 6 Comparison of estimated monomer current fraction versus time post emission startup for an ionic-liquid ion source with a single porous carbon emitter and polarity alternation of 1 Hz and 10 Hz.

over time, whereas when alternating at 10 Hz the average mass flow rate of the beam decreases over time. The time scale of the species composition transient is also slower when alternating at 1 Hz relative to 10 Hz. Figure 6 shows a comparison of the monomer current fraction between the two cases, again demonstrating the noted differences. The time constant for the monomer current fraction is 6.51 ms for 1 Hz and 0.42 ms for 10 Hz. It is worth noting that the repeatability of these results has not been confirmed, and the cause for the differences in behavior is unclear.

V. Conclusion

This paper presents a numerical tool for quantitative analysis of the species composition of an ionic-liquid ion source beam from time-of-flight data. The tool is an extension of that presented in Ref. [5] through the inclusion of a finite-width energy distribution for primary species in the beam. Potential applications of the tool include studying the angular or transient dependence of the species composition. Results presented here demonstrate the use of the tool for both applications. However, it must be emphasized that the results presented here are preliminary, and the repeatability of the observed dependences has yet to be analyzed.

VI. Acknowledgements

The author would like to thank Paulo C. Lozano and Madeleine R. Schroeder for collecting and providing the experimental time-of-flight data analyzed in this paper. All experimental time-of-flight data were collected in the Space Propulsion Laboratory at the Massachusetts Institute of Technology.

References

[1] Gamero-Castaño, M. and Hruby, V., "Electrospray as a Source of Nanoparticles for Efficient Colloid Thrusters," *Journal of Propulsion and Power*, Vol. 17, No. 5, 2001, pp. 977–987. https://doi.org/10.2514/2.5858.

[2] Miller, C. E. and Lozano, P. C., "Measurement of the Dissociation Rates of Ion Clusters in Ionic Liquid Ion Sources," *Applied Physics Letters*, Vol. 116, 2020, p. 254101. https://doi.org/10.1063/5.0006529.

[3] Mier-Hicks, F. and Lozano, P. C., "Spacecraft-Charging Characteristics Induced by the Operation of Electrospray Thrusters," *Journal of Propulsion and Power*, Vol. 33, No. 2, 2017, pp. 456–467. https://doi.org/10.2514/1.B36292.

[4] Larriba, C., Castro, S., and Fernandez de la Mora, J., "Monoenergetic Source of Kilodalton Ions from Taylor Cones of Ionic Liquids," *Journal of Applied Physics*, Vol. 101, 2007, p. 084303. https://doi.org/10.1063/1.2717858.

[5] Jia-Richards, O., "Quantification of Ionic-Liquid Ion Source Beam Composition from Time-of-Flight Data," *Journal of Applied Physics*, Vol. 132, No. 7, 2022. https://doi.org/10.1063/5.0094699.

[6] Lozano, P., "Energy Properties of an EMI-Im Ionic Liquid Ion Sources," *Journal of Physics D: Applied Physics*, Vol. 39, 2006, pp. 126–134. https://doi.org/10.1088/0022-3727/39/1/020.

[7] Schroeder, M. R., Gallud, X., Bruno, A. R., Jia-Richards, O., and Lozano, P. C., "Angular Properties of Ionic Liquid Electrospray Emitters," *AIAA SciTech Forum*, American Institute of Aeronautics and Astronautics, National Harbor, MD, USA, 2023. https://doi.org/10.2514/6.2023-1408.

[8] Schroeder, M. R., Bruno, A. R., and Lozano, P. C., "Externally Wetted Ionic Liquid Electrospray Transient Emission Characterization," *AIAA SciTech Forum*, American Institute of Aeronautics and Astronautics, San Diego, CA, USA, 2022. https://doi.org/10.2514/6.2022-0037.